RSC Advances

ROYAL SOCIETY OF CHEMISTRY

PAPER

View Article Online
View Journal | View Issue

Check for updates

Cite this: *RSC Adv.*, 2025, **15**, 46266

Triple-synergy bactericidal action: a mannose-decorated bioinspired coating on silver-mesoporous silica for eradicating multidrug-resistant *Mycobacterium tuberculosis*

Yiyan Song, *[a] Dawei Yu,[a] Zhijie Sheng,[a] Huafeng Song,[a] Junchi Xu,[a]
Jianping Zhang,*[b] Hui Chen*[a] and Ping Xu*[a]

Received 17th September 2025
Accepted 12th November 2025

DOI: 10.1039/d5ra07047c

rsc.li/rsc-advances

Tuberculosis, the world's leading cause of death from a single infectious agent in 2023, is exacerbated by the rising prevalence of multidrug-resistant (MDR) *Mycobacterium tuberculosis*, underscoring an urgent need for novel therapeutic agents. In this study, we developed a green *in situ* synthesis strategy for silver nanoparticles (Ag NPs) utilizing polydopamine (PDA) as a biomimetic reducing and coating agent on mesoporous silica (SBA-15). The material was further co-coated with the antimicrobial polymer epsilon-poly-L-lysine (EPL) and functionalized with mannose *via* a Schiff-base reaction. The resulting composite, denoted as Ag@SBA-15/Man-PDA-EPL, was comprehensively characterized by physicochemical techniques and exhibited low cytotoxicity. *Mycobacterium tuberculosis* (H37Rv and MDR) was used for the evaluation of the prepared nanocomposites in which the components (Ag@SBA-15/PDA and EPL) exhibited synergistic effect towards MDR. The mannose-grafted composite (Ag@SBA-15/Man-PDA-EPL) exhibited significantly enhanced anti-tubercular efficacy compared to its non-functionalized counterpart (Ag@SBA-15/PDA-EPL), an improvement attributed to the antibacterial capability conferred by the Schiff-base formation. Transmission electron microscopy (TEM) imaging confirmed extensive cellular damage in mycobacteria treated with Ag@SBA-15/Man-PDA-EPL. This study validates a rational combination strategy integrating silver nanoparticles, EPL, and ligand-specific targeting *via* a Schiff-base moiety into a unified nanoplatform, offering a promising approach to combat drug-resistant tuberculosis and mitigate nosocomial infections.

1 Introduction

Tuberculosis (TB), a disease caused by the bacillus *Mycobacterium tuberculosis* (*M. tuberculosis*), is transmitted *via* airborne droplets when individuals with active pulmonary TB expel bacteria into the air.[1] According to the World Health Organization's Global Tuberculosis Report 2024,[2] an estimated 10.8 million people developed TB globally in 2023, representing a sustained increase from 10.7 million in 2022, 10.4 million in 2021 and 10.1 million in 2020. In 2023, TB re-established itself as the world's foremost cause of death from a single infectious agent, a position it had temporarily yielded to coronavirus disease (COVID-19) during the preceding three years. A critical challenge in TB control is drug resistance, the estimated proportion of new TB cases exhibiting multidrug- or rifampicin-resistance (MDR/RR-TB) was 3.2% in 2023, while among previously treated cases, this figure rose markedly to 16%.[2,3] The persistent and evolving threat of drug-resistant *M. tuberculosis* strains continues to constitute a serious public health crisis,[4–6] necessitating the urgent development of new and effective antibacterial agents.

Due to the increasing prevalence of drug-resistant tuberculosis, the development of novel antimicrobial agents has become an urgent priority.[7] Silver-based nanomaterials represent a promising supplement to conventional antibiotics, owing to their demonstrated efficacy against resistant bacterial strains.[8] Silver nanocomposites contain many types including metallic silver nanoparticles, silver salts, silver oxide and so on.[9] Among them, metallic silver nanoparticles are generally the most suitable for antibacterial applications, attributed to providing a sustained release of antibacterial silver ions, and ensuring long-lasting activity.[10] The antimicrobial mechanisms of these nanomaterials include disruption of bacterial metabolic processes, interaction with microbial DNA, and increased permeability of the cytoplasmic membrane.[11] N Kiria *et al.* reported that the combination of rifampicin and silver nanocomposites led to complete suppression of *Mycobacterium tuberculosis* growth in 51.4% of rifampicin-resistant TB

---

[a] *Department of Clinical Laboratory, The Fifth People's Hospital of Suzhou, The Affiliated Infectious Diseases Hospital of Soochow University, Suzhou, 215000, China. E-mail: songyiyan94@163.com; huihuich12@126.com; 573311485@qq.com*

[b] *Department of Tuberculosis, The Fifth People's Hospital of Suzhou, The Affiliated Infectious Diseases Hospital of Soochow University, 215000, China. E-mail: zhangjianping_yb@suda.edu.cn*

strains.[12] Similarly, Teona Avaliani *et al.* demonstrated that the addition of a 2.5% silver nanocomposite solution to a standard dose of moxifloxacin enhanced the minimal inhibitory effect against moxifloxacin-resistant *M. tuberculosis* in 86.7% of cases *in vitro*.[13] These findings underscore the potential of silver nanocomposites to potentiate the activity of existing clinical drugs and counteract drug resistant *M. tuberculosis*.

Despite the promising anti-tuberculosis potential of silver nanocomposites, their toxicity is considered in light of further biomedical applications, such as the toxicity of substances used in the synthesis process and their potential harm to human health and the environment.[10,14] To address this issue, encapsulating them within a carrier vehicle can enable more targeted delivery and reduce systemic exposure to metallic nanoparticles. Mesoporous silica such as Santa Barbara Amorphous-15 (SBA-15),[15] Mobil Composition of Matter-41 (MCM-41),[16] and Korea Advanced Institute of Science and Technology-6 (KIT-6)[17] with the diameters of pores ranging from 2 to 50 nm, have attracted significant attention in nanomedicine due to their excellent biocompatibility.[18,19] For instance, Chee *et al.* used mesoporous silica as a carrier to enhance the oral delivery of poorly soluble anti-tuberculosis drugs, significantly improving the solubility.[20] Bastian *et al.* demonstrated that mesoporous silica as a carrier system greatly enhanced the cellular uptake and subsequent antimycobacterial activity against intracellular *M. tuberculosis*.[21] Among these, SBA-15 with a size within the range of a few micrometers is particularly noteworthy for its highly ordered hexagonal pore structure with pore size of 5–30 nm, thick pore walls, and abundant surface silanol groups, which facilitate functionalization and make it an attractive platform for the delivery of pharmaceutical molecules.[22]

As a mussel-inspired material derived from mussel adhesion proteins, polydopamine (PDA) exhibited excellent adhesion to virtually all types of substrates.[23] Rich in catechol and amine groups, PDA allows for post-functionalization with metal nanoparticles, polymers and polypeptides.[24] Owing to its simple preparation, outstanding biocompatibility, and low cytotoxicity, PDA has been widely employed in various fields such as biomaterials, energy, and catalysis.[25,26] PDA can also serve as a green material for the synthesis of silver nanoparticles, and the resulting nanoparticles demonstrate enhanced compatibility for biomedical applications. Notably, the amino acid sequence of mussel foot protein *Mefp-5* contains both L-dopamine and lysine.[23] Composed of basic amino acid lysine, epsilon-poly-L-lysine (EPL) possesses a wide-spectrum antimicrobial property.[27] As a naturally sourced and low-cost polymer, EPL is extensively used as a food preservative and is recognized as safe by the Food and Drug Administration (FDA).[28] The abundant amino groups in both PDA and EPL facilitate the formation of C=N bonds (Schiff bases), which have demonstrated antibacterial properties. Therefore, PDA and EPL with relatively good biocompatibility are suitable for surface modification.

In the aspect of anti-tuberculosis therapy, a major challenge is the off-target of antimicrobial agents, leading to suboptimal therapeutic outcomes. *Mycobacterium tuberculosis* predominantly resides within macrophages and can cause macrophages to become dormant, thereby preventing antimicrobial drugs from entering and exerting anti-tuberculosis effects.[29,30] The mannose receptor, also known as CD206, is highly expressed on dormant macrophages and mediates the phagocytosis or endocytosis of mannosylated compounds, playing an important role in host immune responses.[31,32] Meanwhile, mannose can be conjugated to material surfaces *via* Schiff base reactions to enhance targeting and antibacterial efficacy.[33] Thus, mannosylated nanocomposites can serve as effective cargo to deliver active constituents specifically to dormant macrophages, thereby improving anti-tuberculosis efficacy.

In this study, we aimed to synthesize silver nanoparticles through *in situ* reduction of silver ions within self-polymerized polydopamine (PDA) coatings on mesoporous silica SBA-15, while simultaneously co-coating the mesopores with epsilon-poly-L-lysine (EPL). Mannose was subsequently grafted as a target recognition molecule *via* Schiff base reaction. The resulting composites, denoted as Ag@SBA-15/Man-PDA-EPL, exhibited improved anti-tuberculosis performance attributed to the triple bactericidal effect of silver nanoparticles, EPL and Schiff base. Besides, the optimal component ratios within the composite were systematically investigated to maximize anti-tuberculosis performance. The physicochemical methods and cytotoxicity test were used to characterize the Ag@SBA-15/Man-PDA-EPL composites.

2 Materials and methods

2.1 Materials

Dopamine hydrochloride was sourced from Aladdin Industrial Corporation (Shanghai, China). Tetraethyl orthosilicate (TEOS), mannose (Man), epsilon-poly-L-lysine (EPL), and silver nitrate ($AgNO_3$) were purchased from the Sinopharm Chemical Reagent Co., Ltd (China). 1-(3-Dimethylaminopropyl)-3-ethylcarbodiimide hydrochloride (EDC·HCl), *N*-hydroxysuccinimide (NHS) and poly(ethylene glycol)-*block*-poly(-propylene glycol)-*block*-poly(-ethylene glycol) ($EO_{20}PO_{70}EO_{20}$, Pluronic P123 with a molecular weight of 5800) were obtained from Sigma-Aldrich (Germany). All reagents were of analytical grade and used without further purification.

2.2 Synthesis of silver-incorporated polydopamine-coated SBA-15 (Ag@SBA-15/PDA)

Ag@SBA-15/PDA was synthesized based on a previously reported method with minor modifications.[34] The preparation of SBA-15 was carried out as follows. Briefly, 4.0 g of P123 was first dissolved in 80 mL of ultrapure water under stirring for 3 h. Then, 70 mL of HCl (3.4 M) was supplied, followed by the addition of 9.14 mL of tetraethyl orthosilicate (TEOS). The mixture was stirred for 24 h at room temperature. Subsequently, the solution was transferred into a Teflon autoclave and subjected to hydrothermal treatment at 100 °C for 24 h. The resulting product was collected by filtration, dried at 80 °C for 24 h, and then calcined at 550 °C for 6 h to remove the surfactant template.

To prepare polydopamine-coated SBA-15 (SBA-15/PDA), 50 mg of SBA-15 was dispersed in 30 mL of tris–HCl buffer

(10 mM, pH 8.5) containing 20 mg of dopamine hydrochloride using ultrasonication for 24 h. The resulting precipitate was achieved by centrifugation and drying. Subsequently, 2 mL of $AgNO_3$ solution (32 mM) was added dropwise to a suspension of SBA-15/PDA (40 mg, 30 mL) maintained at 80 °C under continuous stirring for 12 h. The final product, Ag@SBA-15/PDA, was obtained after washing and drying.

2.3 Synthesis of silver-incorporated mannose coupling polydopamine/EPL-coated SBA-15 (Ag@SBA-15/Man-PDA-EPL)

50 mg of Ag@SBA-15/PDA was mixed with 10–20 mg of EPL in 30 mL of tris–HCl solution (10 mM, pH 7.0) and stirred for 24 h at room temperature. The resulting precipitate was collected and dried to obtain Ag@SBA-15/PDA-EPL. Subsequently, 50 mg of Ag@SBA-15/PDA-EPL was reacted with 5 mg of mannose in the presence of EDC/NHS to facilitate conjugation. The final product was washed thoroughly with ultrapure water, isolated by centrifugation, and dried at 60 °C. The resulting Schiff-base functionalized composite was designated as Ag@SBA-15/Man-PDA-EPL.

2.4 Characterization

Ag@SBA-15/Man-PDA-EPL with the optimal ratio of anti-tuberculosis components was used for the further characterization. Transmission electron microscopy (TEM) was conducted using Hitachi HT-7800 electron microscope operated at an accelerating voltage of 120.0 kV. X-ray photoelectron spectroscopy (XPS) was carried out on a Shimadzu AXIS ULTRA DLD system to evaluate the elementary composition of the samples. X-ray diffraction (XRD) patterns were acquired from a Bruker D8 Advance diffractometer equipped with a rotating anode and Cu Kα radiation ($\lambda = 0.154$ nm). Raman spectroscopy was performed on a Brucker RAM II Raman Spectrometer. Fourier transform infrared (FT-IR) spectra were collected on a Thermo Fourier Nicolet IS50 spectrophotometer.

2.5 Culture of mycobacterial strain

The multidrug-resistant strain (MDR) of *Mycobacterium tuberculosis* (*M. tuberculosis*) was isolated from TB patients at the Affiliated Infectious Diseases Hospital of Soochow University. Strains exhibiting resistance to both rifampin and isoniazid were classified as MDR. The drug-susceptible reference strain H37Rv (ATCC 27294) was also used in this study. MDR and H37Rv strains were both cultured in Middlebrook 7H9 medium (Solarbio, China) supplemented with 10% OADC (Oleic Albumin Dextrose Catalase, Solarbio, China) and on silid Middlebrook 7H10 ager medium (Middlebrook 7H9 medium supplied with agar). All procedures involving *M. tuberculosis* culture were conducted in a Biosafty level 2+ laboratory equipped with negative-pressure containment.

2.6 Optimization the ratio of anti-tuberculosis components

To determine the optimal anti-tuberculosis activity of Ag@SBA-15/PDA in combination with EPL, various amounts of Ag@SBA-15/PDA (0, 0.5, 1, and 2 mg) and EPL (0, 0.2, and 2 mg) were mixed with 10 μL of $\sim10^6$ CFU mL^{-1} suspension of H37Rv strain of *M. tuberculosis*. The mixtures were uniformly spread onto Middlebrook 7H10 agar plates. After incubating at 37 °C for 4–8 weeks, the optimal proportion of Ag@SBA-15/PDA and EPL to inhibit *M. tuberculosis* growth was confirmed according to the colony counts. The images of plates were captured by digital camera. The experiments were performed in triplicate. The survival rates were shown as mean ± SD. A statistical comparison of the survival rates of different groups was performed using one-way analysis of variance (ANOVA). *P* values of <0.05 were considered significant. All statistical analyses were performed using SPSS.

2.7 Minimum inhibitory concentration (MIC) test

The minimum inhibitory concentrations (MICs) of Ag@SBA-15/PDA, Ag@SBA-15/PDA-EPL, Man and Ag@SBA-15/Man-PDA-EPL against *M. tuberculosis* were determined using the microplate Alamar Blue assay. Briefly, 100 μL of each nanocomposite, at the concentrations of 4 to 512 μg mL^{-1} of Ag@SBA-15/PDA, Ag@SBA-15/PDA-EPL and Ag@SBA-15/Man-PDA-EPL, and 32 to1024 μg mL^{-1} of Man were added to individual wells. Subsequently, 100 μL of a suspension of *M. tuberculosis* adjusted to a turbidity equal to 1.0 McFarland standard ($\sim3 \times 10^8$ CFU mL^{-1}) was introduced into each well. The plates were incubatd at 37 °C for 5 days, after which 10 μL of Alamar Blue reagent (Solarbio, China) was supplied, followed by an additional 2 days of incubation. The nanocomposite-free well was considered as positive control while *M. tuberculosis*-free was considered as negative control. The development of a pink color indicated bacterial growth, whereas a blue color signified inhibition. The MIC value was defined as the lowest concentration preventing a color change from blue to pink. To account for the intrinsic color of the nanocomposites and media, control wells without Alamar Blue reagent were included for each concentration. Furthermore, the interaction between Ag@SBA-15/PDA and EPL was evaluated based on the calculation of fractional inhibitory concentration index (FICI)[35] according to the following equation:

$$\text{FICI} = a/A + b/B$$

where *a* represents the MIC value of Ag@SBA-15/PDA in combination with EPL at concentration *b*, *A* stands for the MIC value of Ag@SBA-15/PDA alone, and *B* represents the MIC value of EPL alone. Accordingly, $\text{FICI} \leq 0.5$ means a synergistic effect; $\text{FICI} > 4$ represents the antagonism, and $0.5 < \text{FICI} \leq 4$ represents indifference. The experiments were performed in triplicate. A statistical comparison of MIC values was performed using one-way analysis of variance (ANOVA). *P* values of <0.05 were considered significant. All statistical analyses were performed using SPSS.

2.8 Morphologic alternations in anti-tuberculosis process

The effect of Ag@SBA-15/Man-PDA-EPL on the cellular morphology of MDR strains of *M. tuberculosis* was investigated using TEM. MDR strains of *M. tuberculosis* incubated at 37 °C for 14 days were adjusted to proximately 1×10^8 CFU mL^{-1}. The bacterial suspension was then treated with 16 μg mL^{-1} Ag@SBA-15/Man-PDA-EPL and incubated for 3, 5 and 7 days, respectively. Phosphate-buffered saline (PBS) was used as a negative control. After treatment, the samples were collected by centrifugation, washed, and fixed with 2.5% glutaraldehyde in 0.1 M phosphate buffer (pH 7.4) for 2 h at 4 °C. Finally, the fixed samples were placed on copper grids and measured by a Hitachi HT-7800 transmission electron microscope. A minimum of 20 independent fields of view were randomly analyzed.

2.9 Cell culture and cell viability assay

The MH-S mouse alveolar macrophage cell line was purchased from Shanghai Zhong Qiao Xin Zhou Biotechnology Co., Ltd. MH-S cells were cultured in RPMI-1640 media supplied with 10% (v/v) fetal bovine serum (FBS), 1% (v/v) streptomycin-penicillin and 0.05 mM β-Mercaptoethanol (Shanghai Zhong Qiao Xin Zhou, China) at 37 °C in 5% CO_2 atmosphere. Cytotoxicity was evaluated using a Cell Counting Kit-8 (CCK-8) assay. Briefly, MH-S cells were seeded into 96-well plates at a density of 5000 cells per well and cultured overnight. The cells were then treated with series of concentrations (50, 100, 200, 400, 800 and 1600 μg mL^{-1}) of Ag@SBA-15/Man-PDA-EPL suspension, respectively. After incubation for 24 h, the medium was aspirated, and the cells were gently washed with PBS. Subsequently, 100 μL of fresh media containing 10 μL of CCK-8 solution (Beyotime) was added to each well. After incubation for 2 h, the absorbance at 450 nm was measured by a Thermo Labserv K3 microplate reader. The cell viability (%) of Ag@SBA-15/Man-PDA-EPL was calculated as follows.

$$\text{Cell viability (\%)} = A/A_0 \times 100$$

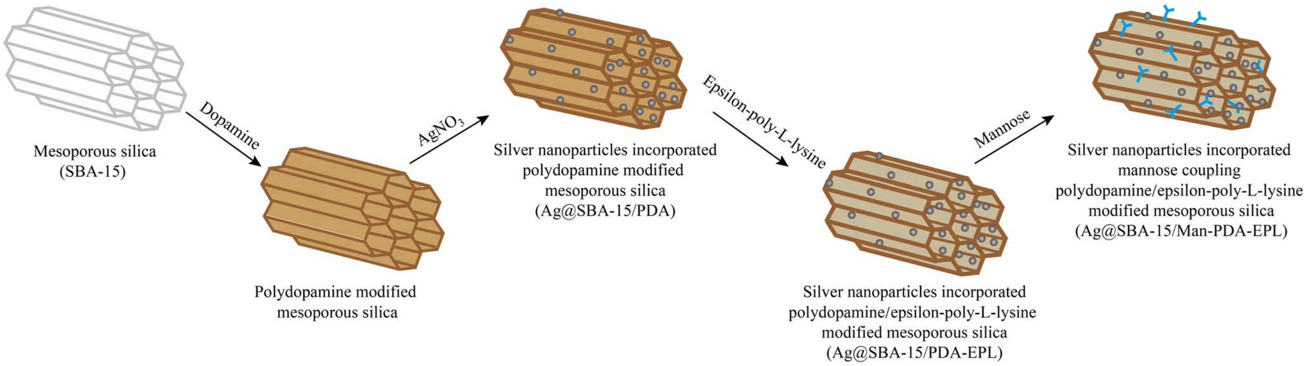

Scheme 1 Synthetic illustration for silver nanoparticles incorporated mannose coupling polydopamine/epsilon-poly-L-lysine modified mesoporous silica (Ag@SBA-15/Man-PDA-EPL).

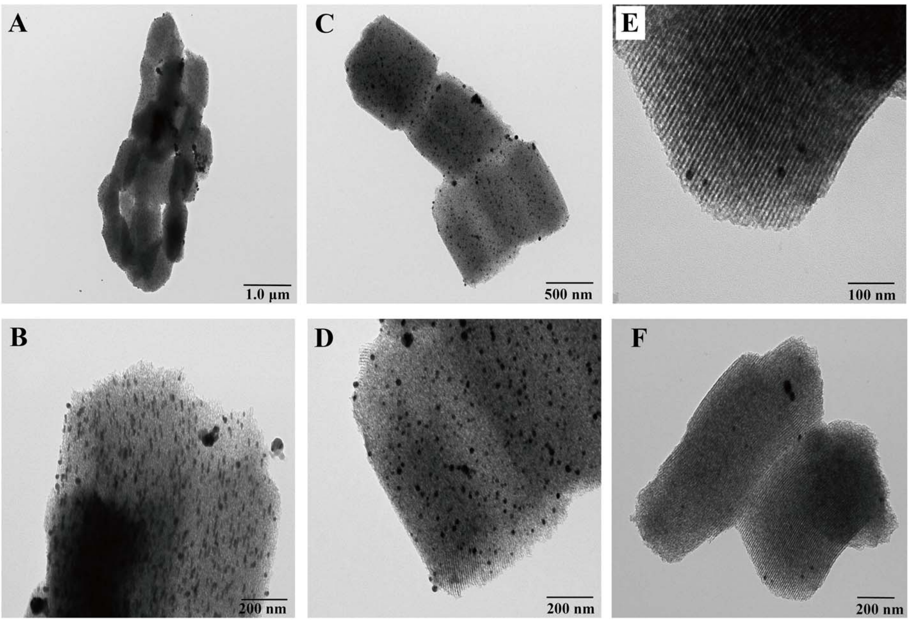

Fig. 1 TEM images of (A and B) Ag@SBA-15/PDA, (C and D) Ag@SBA-15/PDA-EPL and (E and F) Ag@SBA-15/Man-PDA-EPL.

where A_0 means the absorbance of untreated cells and A represents the absorbance in the presence of specific concentration of Ag@SBA-15/Man-PDA-EPL. A statistical comparison of the cell viability of the untreated-group and groups treated with different concentrations of Ag@SBA-15/Man-PDA-EPL was performed using one-way analysis of variance (ANOVA). *P* values of <0.05 were considered significant. All statistical analyses were performed using SPSS.

3 Results and discussion

3.1 Synthesis of Ag@SBA-15/Man-PDA-EPL

The fabrication process of the polydopamine-modified mesoporous silica (SBA-15/PDA) used as a delivery platform for silver and epsilon-poly-L-lysine (EPL) is illustrated in Scheme 1. SBA-15 was typical with the hexagonal channel structure. A polydopamine (PDA) coating was formed through the polymerization of dopamine on both the internal and external surfaces of the SBA-15 mesopores. Silver ions were subsequently reduced *in situ* on the PDA layer. EPL was then co-immobilized onto the PDA-modified surface *via* hydrogen bonding. Finally, mannose (Man) was conjugated to the PDA and EPL through a Schiff-base reaction.

3.2 Characterization

TEM was employed to characterize the morphology of the synthesized materials. As depicted in Fig. 1, Ag@SBA-15/PDA, Ag@SBA-15/PDA-EPL and Ag@SBA-15/Man-PDA-EPL all possessed a rod-like morphology with well-ordered mesostructures. The average pore size of the synthesized SBA-15 is approximately 7.0 nm (Fig. S1). Silver nanoparticles stabilized by PDA were uniformly distributed on the surfaces of Ag@SBA-15/PDA, Ag@SBA-15/PDA-EPL and Ag@SBA-15/Man-PDA-EPL. The formation of silver nanoparticles is attributed to the reducing capability of PDA, which effectively converts silver ions into metallic silver. The silver nanoparticles on Ag@SBA-15/PDA were line-shaped with the average width of 18.3 ± 1.2 nm, and the silver nanoparticles on Ag@SBA-15/PDA-EPL were spherical with the average diameter of 20.5 ± 1.3 nm (observed grain size statistics). Notably, in comparison to Ag@SBA-15/PDA and Ag@SBA-15/PDA-EPL, Ag nanoparticles on Ag@SBA-15/Man-PDA-EPL were relatively smaller in size and displayed a more homogeneous distribution in the mesopores. This precise localization and size control are crucial for the antibacterial activity, as the confined silver nanoparticles within the silica pores may act as a sustained-release reservoir of antibacterial Ag$^+$ ions.

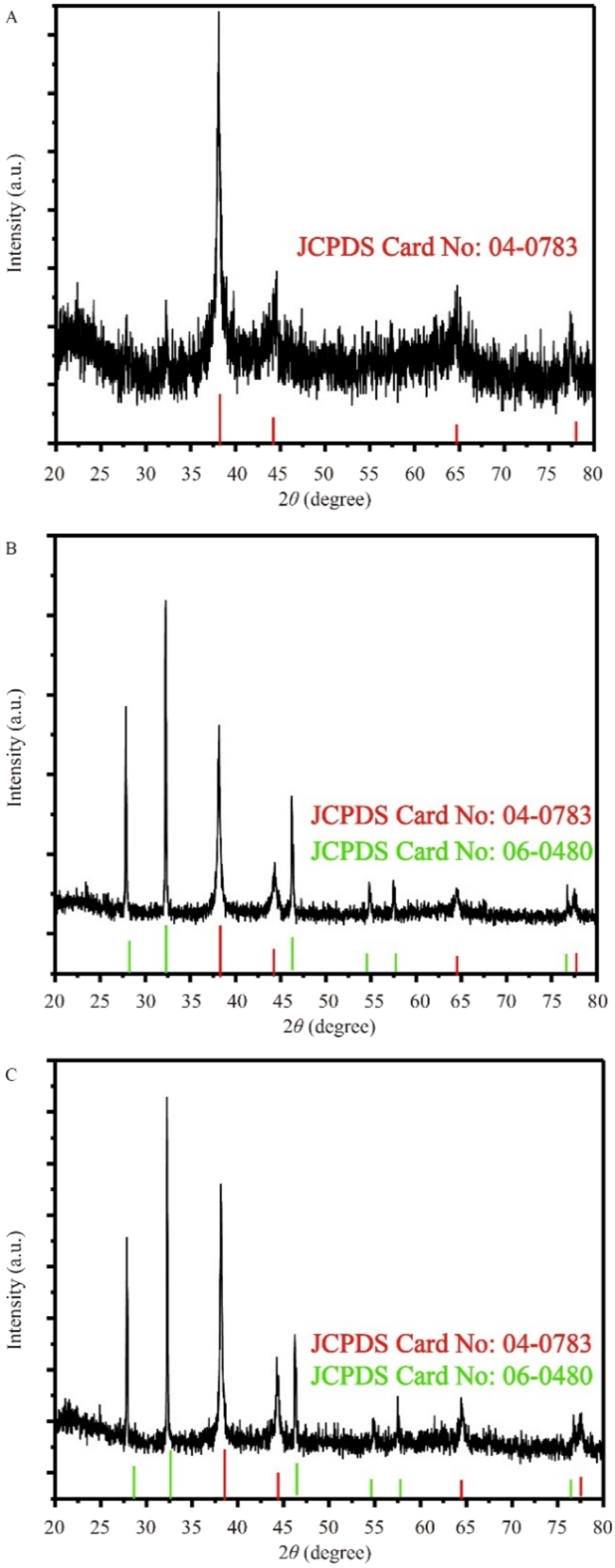

Fig. 2 Wide angle X-ray diffraction patterns of (A) Ag@SBA-15/PDA, (B) Ag@SBA-15/PDA-EPL and (C) Ag@SBA-15/Man-PDA-EPL.

The wide angle XRD patterns of Ag@SBA-15/PDA, Ag@SBA-15/PDA-EPL and Ag@SBA-15/Man-PDA-EPL were presented in Fig. 2A–C. For Ag@SBA-15/PDA-EPL and Ag@SBA-15/Man-PDA-EPL composites, the diffraction peaks at 38.13, 44.30, 64.34, and 77.26° can be assigned to the (111), (200), (220), and (311) crystal planes of metallic silver (JCPDS Card No. 04-0783), respectively, indicating the existence of the cubic structure of Ag nanoparticles.[36] Additionally, peaks detected at 27.86, 32.21, 46.29, 54.78, 57.60, and 76.59° corresponded to the (111), (200), (220), (311), (222), and (420) planes of AgCl (JCPDS Card No. 06-0480), respectively, confirming the existence of AgCl particles in both Ag@SBA-15/PDA-EPL and Ag@SBA-15/Man-PDA-EPL composites, likely resulting from the presence of chloride ions in the buffer solution during synthesis.[34]

To identify the functional groups present in the nanocomposites, Fourier transform infrared (FT-IR) spectroscopy was conducted, with the results displayed in Fig. 3A. The characteristic framework vibrations of SBA-15 were observed at 1050, 967, 800, and 450 cm^{-1}.[37] Specifically, the peaks at 1050 and 800 cm^{-1} correspond to the asymmetric and symmetric stretching vibrations of Si–O bonds, respectively, originating from the SiO_4 tetrahedra.[37] The peaks at 967 and 450 cm^{-1} were assigned to Si–OH band and anti-symmetric stretching vibration of the Si–O–Si band, respectively.[37] In the spectrum of Ag@SBA-15/PDA-EPL, two peaks around 1645 and 1550 cm^{-1} are associated with the amide groups of EPL, arising from the stretching vibrations of the N–H, C=O and C–N bonds.[38] Compared with Ag@SBA-15/PDA-EPL, the spectrum of Ag@SBA-15/Man-PDA-EPL appeared a new peak at 1410 cm^{-1} alongside a reduction in the intensity of the 1550 cm^{-1} band, which indicated mannose reacted with PDA and EPL forming Schiff base (C=N bond).[39] Additionally, the obvious wide peaks in the range of 3000–3700 cm^{-1} for Ag@SBA-15/Man-PDA-EPL are assigned to O–H vibration peaks,[39] further confirming the successful grafting of mannose.

Raman spectroscopy, as a powerful nondestructive technique, has been widely used to explore the structure order of carbon-based materials.[40] As shown in Fig. 3B, the Raman spectra of Ag@SBA-15/PDA, Ag@SBA-15/PDA-EPL and Ag@SBA-15/Man-PDA-EPL all exhibit two characteristic peaks at approximately 1406 and 1580 cm^{-1}. These bands correspond to the D band (disorder-induced mode) and G band (in-plane vibrational mode of sp^2-hybridized carbon), respectively, associated with the stretching and deformation vibrations of aromatic rings in the polydopamine layer.[34] The similar intensity ratios of D/G across the composites indicate that the subsequent functionalization with EPL and mannose did not alter the fundamental graphitic structure or defect density of the carbonaceous coating. However, the striking feature is the dramatic signal enhancement observed for the Ag@SBA-15/Man-PDA-EPL composite. This orders-of-magnitude intensity increase, coupled with the unchanged spectral profile, suggests the emergence of a significant Surface-Enhanced Raman Scattering (SERS) effect,[41] likely optimized by the specific size and distribution of the silver nanoparticles on Ag@SBA-15/Man-PDA-EPL.

The chemical composition and surface electronic states of Ag@SBA-15/PDA, Ag@SBA-15/PDA-EPL and Ag@SBA-15/Man-PDA-EPL composites were further recorded by XPS spectra. As given in Fig. S2A, the survey spectra of Ag@SBA-15/PDA, Ag@SBA-15/PDA-EPL and Ag@SBA-15/Man-PDA-EPL exhibited similar profiles, with surface elements primarily consisting of Si, O, Ag, N, and C elements. A distinct Ag signal was observed around 370 eV in Fig. S2A, and the high-resolution Ag 3d spectra (Fig. S2B) displayed two peaks at binding energies of 365.6 eV and 371.5 eV, corresponding to Ag $3d_{5/2}$ and Ag $3d_{3/2}$, respectively.[34] The measured binding energies and the spin–orbit splitting of 5.9 eV are characteristic of metallic silver (Ag^0),[42] which conclusively confirms the successful formation of silver nanoparticles in all samples. Quantitative analysis calculated by XPS revealed that the Ag contents in Ag@SBA-15/PDA, Ag@SBA-15/PDA-EPL and Ag@SBA-15/Man-PDA-EPL composites were 0.87 at% (5.02 wt%), 1.22 at% (6.91 wt%) and 0.59 at% (4.02 wt%), respectively. The higher Ag content in Ag@SBA-15/PDA-EPL suggests that EPL provides additional coordination sites or a stabilizing environment that enhances silver nanoparticles retention or formation. Conversely, the relative low Ag content in Ag@SBA-15/Man-PDA-EPL, despite its more homogeneous distribution observed by TEM (Fig. 1E and F), may be attributed to the mannose functionalization process, which could slightly hinder the reduction or loading efficiency of silver. This indicates that while the surface chemistry (PDA, EPL, mannose) influences the final Ag content and distribution, the metallic state of silver is consistently achieved across all samples. In the O 1s spectra (Fig. S2C), the main peaks were located at 532.92, 532.69 and 532.55 eV for Ag@SBA-15/PDA, Ag@SBA-15/PDA-EPL and Ag@SBA-15/Man-PDA-EPL, respectively. The C 1s spectra were fitted with multiple peaks after subtracting a Tougaard background (Fig. 4A). In the spectrum of Ag@SBA-15/PDA, the bounding energies observed at 284.90 and 288.80 eV correspond to the C–C/C–H and C=O groups of PDA, respectively.[43] For Ag@SBA-15/PDA-EPL, the C 1s spectrum

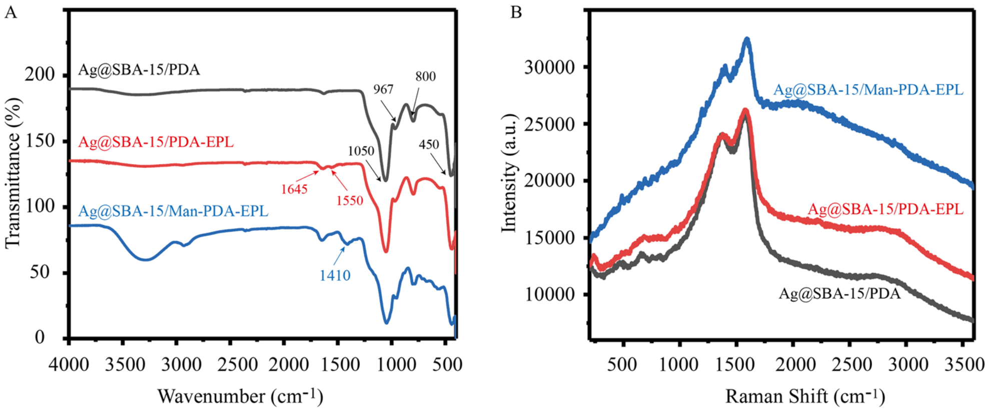

Fig. 3 (A) Fourier Transform Infrared spectra and (B) Raman spectra of Ag@SBA-15/PDA, Ag@SBA-15/PDA-EPL and Ag@SBA-15/Man-PDA-EPL.

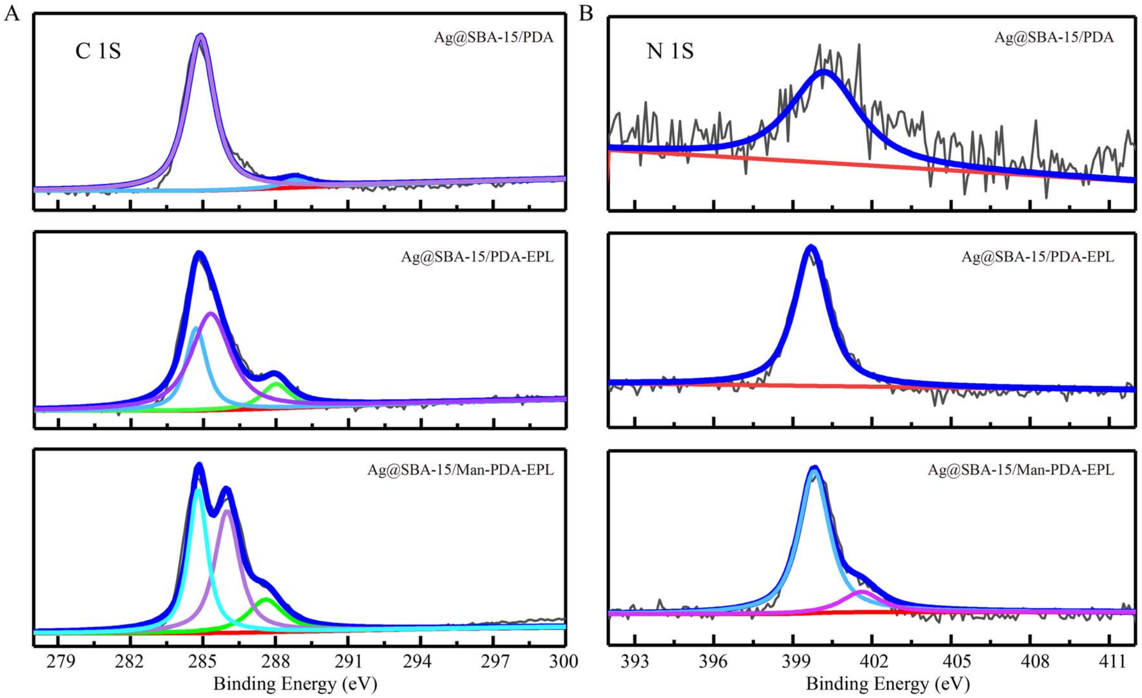

Fig. 4 High-resolution XPS spectra of (A) C 1s and (B) N 1s of Ag@SBA-15/PDA, Ag@SBA-15/PDA-EPL and Ag@SBA-15/Man-PDA-EPL.

exhibited peaks at 284.70, 285.30 and 288.00 eV, which are attributed to C–C/C–H, C–N and C═O groups, respectively.[43] In the case of Ag@SBA-15/Man-PDA-EPL, peaks were identified at 284.80, 286.00 and 287.60 eV, assigned to C–C/C–H, C═N and C═O, respectively.[39] The new presence of the C═N peak suggests the occurrence of a Schiff base reaction between mannose and PDA/EPL. Furthermore, the N 1s spectrum of Ag@SBA-15/PDA showed a peak at 400.2 eV, corresponding to the C–N bond in PDA, while that of Ag@SBA-15/PDA-EPL exhibited a peak at 399.7 eV, assigned to H–N–H.[43] Additionally, the N 1s spectrum of Ag@SBA-15/Man-PDA-EPL in Fig. 4B was deconvoluted into two peaks at 399.81 and 401.60 eV, which may be assigned to H–N–H and C═N, respectively, further supporting the formation of Schiff base.[44]

3.3 Evaluation of the anti-tuberculosis performance

To optimize the anti-tuberculosis efficacy of the combined use of Ag@SBA-15/PDA and EPL, different contents of Ag@SBA-15/PDA and EPL were evaluated for their activity against *M. tuberculosis*. As shown in Fig. 5, 0.2 mg EPL without adding Ag@SBA-15/PDA exhibited negligible anti-tuberculosis effect, while 2 mg of EPL alone can kill 50 ± 1.7% *M. tuberculosis* ($P <$ 0.05, there were statistically significant differences between 0.2 mg and 2 mg EPL-treated groups). When 1 mg and 2 mg of Ag@SBA-15/PDA were used individually, the survival rates of *M. tuberculosis* were approximately 45 ± 2.2% and 20 ± 5.8%, respectively ($P < 0.05$, there were statistically significant differences between 1 mg and 2 mg Ag@SBA-15/PDA-treated groups). In contrast, the combination of 1 mg Ag@SBA-15/PDA and 0.2 mg EPL resulted in complete *M. tuberculosis* eradication. Similarly, a combination of 0.5 mg Ag@SBA-15/PDA and 0.2 mg EPL also achieved full elimination of *M. tuberculosis* ($P > 0.05$, there were no statistically significant differences between 1 mg Ag@SBA-15/PDA + 0.2 mg EPL and 0.5 mg Ag@SBA-15/PDA + 0.2 mg EPL-treated groups). Based on these results, the optimal mass ratio of Ag@SBA-15/PDA to EPL was determined to be 5 : 2, which was subsequently used for the synthesis of Ag@SBA-15/PDA-EPL composites.

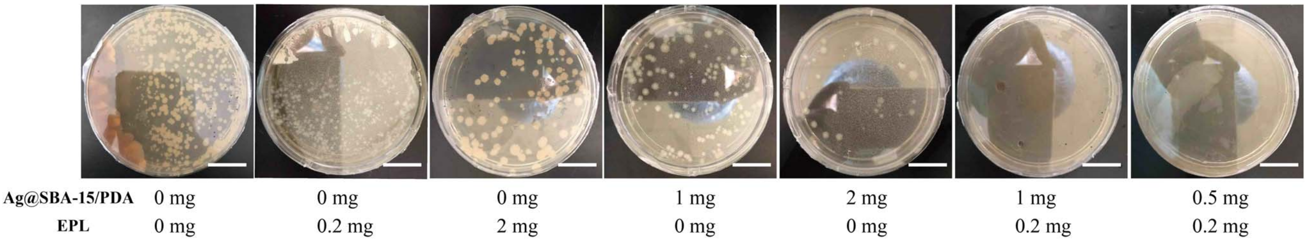

Fig. 5 Images of different contents of Ag@SBA-15/PDA and EPL cultured with *M. tuberculosis* (H37Rv).

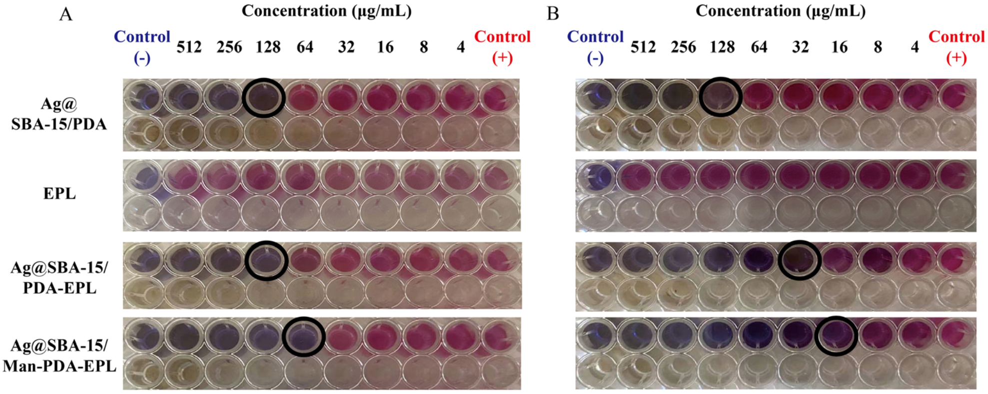

Fig. 6 The MIC results of concentrations of 4–512 μg mL^{-1} of Ag@SBA-15/PDA, EPL, Ag@SBA-15/PDA-EPL and Ag@SBA-15/Man-PDA-EPL against (A) H37Rv and (B) MDR strains of *M. tuberculosis*.

The antimycobacterial activities of Ag@SBA-15/PDA, EPL, Ag@SBA-15/PDA-EPL, mannose, and Ag@SBA-15/Man-PDA-EPL composites were evaluated against both the H37Rv and multidrug-resistant (MDR) strains of *M. tuberculosis* using the microplate Alamar Blue assay. The minimum inhibitory concentrations (MICs) of rifampin and isoniazid against MDR strain were determined to be 64 and 32 μg mL^{-1}, respectively. As shown in Fig. 6, the MIC values of Ag@SBA-15/PDA, EPL, Ag@SBA-15/PDA-EPL and Ag@SBA-15/Man-PDA-EPL against H37Rv were 128, >512, 128 and 64 μg mL^{-1}, respectively (Ag@SBA-15/PDA *vs.* EPL, Ag@SBA-15/PDA *vs.* Ag@SBA-15/Man-PDA-EPL, EPL *vs.* Ag@SBA-15/PDA-EPL, EPL *vs.* Ag@SBA-15/Man-PDA-EPL: $P < 0.05$). Against the MDR strain, the corresponding MIC values were 128, >512, 32 and 16 μg mL^{-1}, respectively (Ag@SBA-15/PDA *vs.* EPL, Ag@SBA-15/PDA *vs.* Ag@SBA-15/PDA-EPL, Ag@SBA-15/PDA *vs.* Ag@SBA-15/Man-PDA-EPL, EPL *vs.* Ag@SBA-15/PDA-EPL, EPL *vs.* Ag@SBA-15/Man-PDA-EPL, Ag@SBA-15/PDA-EPL *vs.* Ag@SBA-15/Man-PDA-EPL: $P < 0.05$). As expected, upon the combination with Ag@SBA-15/PDA and EPL, an improved antimycobacterial effect against MDR strain was achieved. As listed in Table 1, the calculated fractional inhibitory concentration index (FICI) derived from the MIC results revealed a synergistic interaction between Ag@SBA-15/PDA and EPL against MDR strain, whereas the interaction against H37Rv was classified as either synergistic or indifferent. Additionally, mannose alone showed MIC values >1024 μg mL^{-1} against both strains (Fig. S3) (the MICs against H37Rv and MDR of Ag@SBA-15/PDA *vs.* mannose, EPL *vs.* mannose, Ag@SBA-15/PDA-EPL *vs.* mannose, Ag@SBA-15/Man-PDA-EPL *vs.* mannose: $P < 0.05$). In contrast, the MIC values of Ag@SBA-15/Man-PDA-EPL against H37Rv and MDR were 64 and 16 μg mL^{-1}, respectively, both lower than those of Ag@SBA-15/PDA-EPL (128 and 32 μg mL^{-1}). This enhancement may be attributed to the anti-tuberculosis effect of the newly formed Schiff base.[45]

To further verify the anti-tuberculosis effect of Ag@SBA-15/Man-PDA-EPL nanocomposites, morphological changes in multidrug-resistant (MDR) *M. tuberculosis* strains were observed using transmission electron microscopy (TEM). As shown in Fig. 7A, untreated MDR *M. tuberculosis* cells exhibited a typical slender and slightly curved rod-shaped morphology, with an average length of approximately 4 μm. After 5 days of exposure to Ag@SBA-15/Man-PDA-EPL, the bacterial cells became unsmooth (Fig. 7B and C). Following 7 days of treatment, the cellular structure exhibited pronounced roughness and extensive damage, with clear signs of disruption (Fig. 7D). These

Table 1 MIC Values (μg mL^{-1}) of different samples on H37Rv and MDR Strains of *M. tuberculosis* and corresponding FICIs

Strain	Samples	MIC (μg mL^{-1})	The content of Ag@SBA-15/PDA (μg mL^{-1})	The content of EPL (μg mL^{-1})	FICI	Interaction type
H37Rv	Ag@SBA-15/PDA	128	128	0	—	—
	EPL	>512	0	>512	—	—
	Ag@SBA-15/PDA-EPL	128	91.43	36.57	<0.784 (≤4)	Synergy or indifference
	Mannose	>1024	—	—	—	—
	Ag@SBA-15/Man-PDA-EPL	64	—	—	—	—
MDR	Ag@SBA-15/PDA	128	128	0	—	—
	EPL	>512	0	>512	—	—
	Ag@SBA-15/PDA-EPL	32	22.86	9.14	<0.196 (<0.5)	Synergy
	Mannose	>1024	—	—	—	—
	Ag@SBA-15/Man-PDA-EPL	16	—	—	—	—

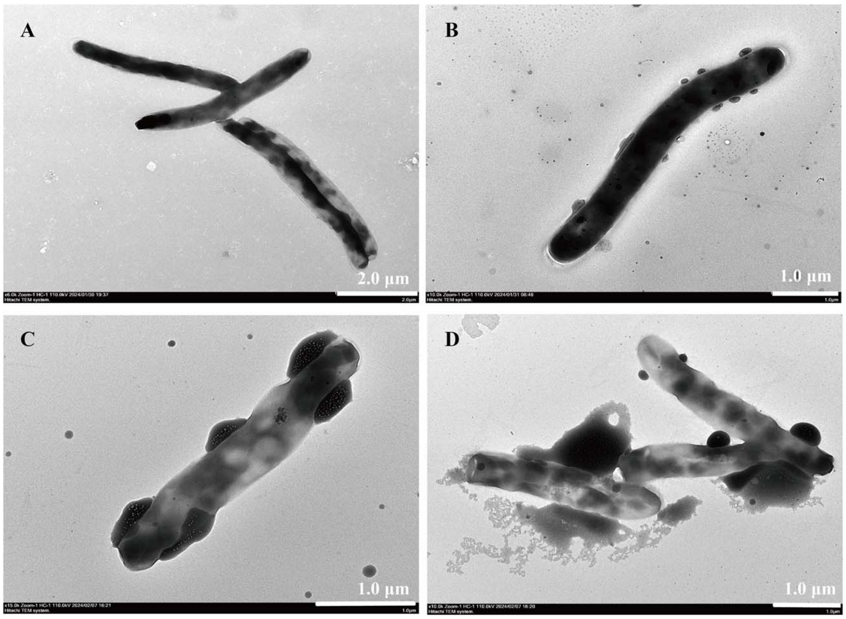

Fig. 7 TEM images of MDR strains of *M. tuberculosis* treated with PBS (A) for 7 days, and treated with Ag@SBA-15/Man-PDA-EPL for 5 days (B and C) and 7 days (D).

morphological alterations are likely attributable to the degradation of the cell wall and mycolic acid layers,[46] closely align with the physical degradation mechanisms widely reported in the literature for silver-based nanomaterials and metal ions, which are known to cause such cellular damage.[47] These findings demonstrate that silver-functionalized silica nanomaterials hold significant promise for biological antibacterial applications. The developed Ag@SBA-15/Man-PDA-EPL nanocomposite effectively kills MDR *M. tuberculosis* through such structural damage, a performance consistent with previously reported results.[48,49] Consequently, the application of Ag@SBA-15/Man-PDA-EPL in clinical settings may help reduce nosocomial infections and mitigate the spread of antibiotic-resistant bacteria.

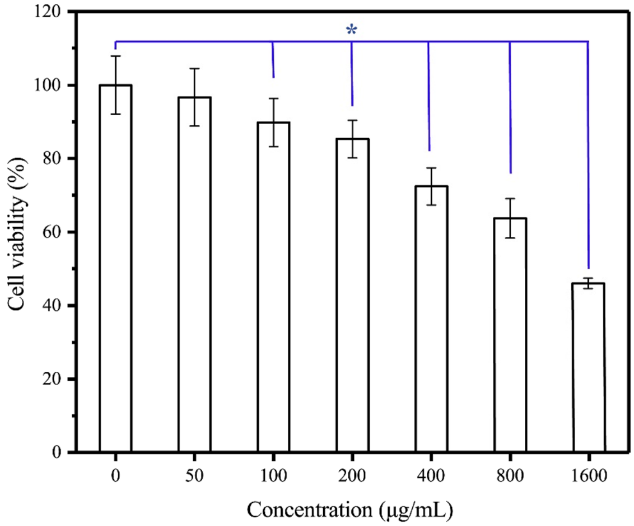

Fig. 8 Cell viability assay of MH-S cells incubation with series of concentrations of Ag@SBA-15/Man-PDA-EPL suspensions. Values are the average of three independent experiments in triplicate and shown as mean ± SD ($n = 3$). Untreated-group *vs.* different concentrations of Ag@SBA-15/Man-PDA-EPL treated groups at $P < 0.05$ level (*).

3.4 Cytotoxicity analysis

The potential toxicity of the nanocomposites is a major consideration in practice. To evaluate the latent toxicity of synthesized Ag@SBA-15/Man-PDA-EPL, mouse alveolar macrophage cell line MH-S cells were exposed to varying concentrations of the nanocomposite suspension for 24 h. As shown in Fig. 8, at concentrations up to 100 $\mu g\ mL^{-1}$, which exceeds the MIC values against both H37Rv (64 $\mu g\ mL^{-1}$) and MDR strains (16 $\mu g\ mL^{-1}$) of *M. tuberculosis*, the viability of MH-S cells remained above 90%, demonstrating low cytotoxicity of Ag@SBA-15/Man-PDA-EPL toward MH-S cells. These results indicate that silver nanoparticles incorporated mannose coupling polydopamine/epsilon-poly-L-lysine modified mesoporous silica composites exhibits favorable biocompatibility and represents a promising candidate for anti-tuberculosis applications.

4 Conclusions

In summary, silver nanoparticles were facilely synthesized *in situ* under mild conditions assisted by mussel-inspired polydopamine adhesive on SBA-15, with the co-loading of antibacterial polymer epsilon-poly-L-lysine. Mannose was subsequently grafted onto the composite *via* Schiff base (C═N) formation through reaction with PDA/EPL. The synthesized Ag@SBA-15/Man-PDA-EPL composites retained the mesoporous structure and were decorated with the silver nanoparticles, while the successful formation of the Schiff base was confirmed by FT-IR and XPS analyses. The optimal anti-tuberculosis mass ratio of Ag@SBA-15/PDA to EPL was determined to be 5 : 2, and MIC evaluations revealed a synergistic effect between ingredient Ag@SBA-15/PDA and EPL in Ag@SBA-15/PDA-EPL against MDR strain of *M. tuberculosis*. The observed synergy between Ag@SBA-15/PDA and EPL is consistent with the established concept of combining metallic nanoparticles with cationic polymers to potentiate antibacterial activity, as reported in studies on other bacterial systems.[50] Besides, compare with Ag@SBA-15/PDA-EPL, Ag@SBA-15/Man-PDA-EPL exhibited superior anti-tuberculosis property, which may be attributed to the additional antibacterial effect of the grafted Schiff base. This enhanced efficacy aligns with the intrinsic antibacterial properties of Schiff bases, particularly those derived from monosaccharides like mannose, which have been reported to disrupt the membrane integrity.[45] Furthermore, TEM observations suggested that Ag@SBA-15/Man-PDA-EPL made the structural cellular damage of *M. tuberculosis*. Taken together, the constructed Ag@SBA-15/Man-PDA-EPL composites exhibit low cytotoxicity and combine the triple bactericidal effects of silver nanoparticles, EPL, and the Schiff base, offering a promising strategy to combat drug-resistant *M. tuberculosis* and demonstrating significant potential for biomedical applications.

Ethical statement

All experiments involving the multidrug-resistant strain of *Mycobacterium tuberculosis* isolated from TB patients were performed in accordance with the Guidelines of the National Health Commission of the People's Republic of China and the Helsinki Declaration. These experiments were reviewed and approved by the Ethics Committee of ffiliated Infectious Diseases Hospital of Soochow University (Approval No. K-2025-002-01). Informed consent was obtained from all human participants prior to their participation in this study.

Author contributions

Conceptualization, Yiyan Song, Dawei Yu, Hui Chen and Ping Xu; data curation, Yiyan Song and Huafeng Song; formal analysis, Yiyan Song, Dawei Yu and Junchi Xu; funding acquisition, Yiyan Song, Jianping Zhang, Hui Chen and Ping Xu; investigation, Yiyan Song; methodology, Yiyan Song, Dawei Yu and Zhijie Sheng; project administration, Yiyan Song; resources, Huafeng Song, Jianping Zhang and Hui Chen; software, Zhijie Sheng and Huafeng Song; supervision, Yiyan Song; validation, Dawei Yu and Junchi Xu; visualization, Dawei Yu and Huafeng Song; writing – original draft, Yiyan Song and Hui Chen; writing – review & editing, Jianping Zhang and Ping Xu.

Conflicts of interest

The authors declare no conflict of interest.

Data availability

The authors declare that all the data will be made available upon reasonable request.

Supplementary information (SI): Fig. S1: TEM image of SBA-15. Fig. S2: (A) XPS spectra of Ag@SBA-15/PDA, Ag@SBA-15/PDA-EPL and Ag@SBA-15/Man-PDA-EPL, and high-resolution spectra of (B) Ag 3d and (C) O 1s of Ag@SBA-15/PDA, Ag@SBA-15/PDA-EPL and Ag@SBA-15/Man-PDA-EPL. Fig. S3: the MIC results of concentrations of 32–1024 μg mL^{-1} of mannose against H37Rv and MDR strains of *M. tuberculosis*. See DOI: **https://doi.org/10.1039/d5ra07047c**.

Acknowledgements

This work was financially supported by Jiangsu Provincial Health Commission Project (MQ2024024 and K2024075), Key Research and Development Project of Jiangsu Provincial Department of Science and Technology (BE2023718), Suzhou Science and Technology Project (SYW2025152 and SYW2025021), and the Boxue Fund National Natural Science Foundation (Youth Innovation Project) of the Fifth People's Hospital of Suzhou (BOXUE2024002).

References

1 S. T. Cole, R. Brosch, J. Parkhill, T. Garnier, C. Churcher, D. Harris, S. V. Gordon, K. Eiglmeier, S. Gas, C. E. Barry III, F. Tekaia, K. Badcock, D. Basham, D. Brown, T. Chillingworth, R. Connor, R. Davies, K. Devlin, T. Feltwell, S. Gentles, N. Hamlin, S. Holroyd, T. Hornby, K. Jagels, A. Krogh, J. McLean, S. Moule, L. Murphy, K. Oliver, J. Osborne, M. A. Quail, M. A. Rajandream, J. Rogers, S. Rutter, K. Seeger, J. Skelton, R. Squares, S. Squares, J. E. Sulston, K. Taylor, S. Whitehead and B. G. Barrell, *Nature*, 1998, **393**, 537.

2 *Global tuberculosis report 2024*, World Health Organization, Geneva, 2024, Licence: CC BY-NC-SA 3.0 IGO.

3 K. Dheda, F. Mirzayev, D. M. Cirillo, Z. Udwadia, K. E. Dooley, K. C. Chang, S. V. Omar, A. Reuter, T. Perumal, C. R. Horsburgh Jr, M. Murray and C. Lange, *Nat. Rev. Dis. Primers*, 2024, **10**, 22.

4 X. Y. Lu, Y. Jiang, Y. P. Liu, J. H. Chen, Y. L. Lao, J. Li, Y. Y. Zhang, N. Li, L. L. Wang, C. L. Yu, Q. Ye, W. Wei, J. L. Deng, X. Shen and C. G. Yang, *Emerg. Microb. Infect.*, 2025, **14**, 2521842.

5 N. Wang, F. R. Meng, L. Deng, L. Wu, Y. Yang, H. Li, Y. J. Chen, Z. Y. Wei, B. Xie, L. Gong, Q. Niu, J. Lei, J. W. Gao, B. Huang, Q. Wang, X. M. Lai, Z. H. Liu and J. X. Hu, *Emerg. Microb. Infect.*, 2025, **14**, 2447607.

6 G. A. Goig, C. Loiseau, N. Maghradze, K. McHedlishvili, T. Avaliani, D. Brites, S. Borrell, R. Aspindzelashvili, Z. Avaliani, M. Kipiani, N. Tukvadze, L. Jugheli and S. Gagneux, *N. Engl. J. Med.*, 2025, **392**, 97–99.

7 S. Njikan, S. Ahmed, A. Manning, D. Awasthi, Y. Ovechkina, S. Chowdhury, A. Butts and T. Parish, *Microbiol. Spectr.*, 2022, **10**(3), e01161.

8 G. Franci, A. Falanga, S. Galdiero, L. Palomba, M. Rai, G. Morelli and M. Galdiero, *Molecules*, 2015, **20**, 8856–8874.

9 A. Hamad, K. S. Khashan and A. Hadi, *J. Inorg. Organomet. Polym. Mater.*, 2020, **30**, 4811–4828.

10 E. O. Mikhailova, *Antibiotics*, 2025, **14**, 5.

11 I. X. Yin, J. Zhang, I. S. Zhao, M. L. Mei, Q. L. Li and C. H. Chu, *Int. J. Nanomed.*, 2020, **15**, 2555–2562.

12 N. Kiria, T. Avaliani, N. Bablishvili, G. Phichkhaia and N. Kiria, *Eur. Respir. J.*, 2023, **62**, PA1053.

13 T. Avaliani, N. Kiria, G. Phichkhaia, N. Bablishvili and N. Kiria, *Eur. Respir. J.*, 2023, **62**, PA4545.

14 P. H. Nie, Y. Zhao and H. Y. Xu, *Ecotoxicol. Environ. Saf.*, 2023, **253**, 114636.

15 D. Y. Zhao, J. L. Feng, Q. S. Huo, N. Melosh, G. H. Fredrickson, B. F. Chmelka and G. D. Stucky, *Science*, 1998, **279**, 548–552.

16 J. S. Beck, J. C. Vartuli, W. J. Roth, M. E. Leonowicz, C. T. Kresge, K. D. Schmitt, C. T. W. Chu, D. H. Olson, E. W. Sheppard, S. B. McCullen, J. B. Higgins and J. L. Schlenker, *J. Am. Chem. Soc.*, 1992, **114**, 10834–10843.

17 K. Soni, B. S. Rana, A. K. Sinha, A. Bhaumik, M. Nandi, M. Kumar and G. M. Dhar, *Appl. Catal., B*, 2009, **90**, 55–63.

18 T. I. Janjua, Y. X. Cao, F. Kleitz, M. Linden, C. Z. Yu and A. Popat, *Adv. Drug Delivery Rev.*, 2023, **203**, 115115.

19 P. Kazemzadeh, K. Sayadi, A. Toolabi, J. Sayadi, M. Zeraati, N. P. S. Chauhan and G. Sargazi, *Front. Chem.*, 2022, **10**, 823785.

20 C. W. Ang, L. Tan, Z. Qu, N. P. West, M. A. Cooper, A. Popat and M. A. T. Blaskovich, *ACS Biomater. Sci. Eng.*, 2022, **8**, 4196–4206.

21 B. Beitzinger, F. Gerbl, T. Vomhof, R. Schmid, R. Noschka, A. Rodriguez, S. Wiese, G. Weidinger, L. Standker, P. Walther, J. Michaelis, M. Linden and S. Stenger, *Adv. Healthcare Mater.*, 2021, **10**, e2100453.

22 A. Popat, S. B. Hartono, F. Stahr, J. Liu, S. Z. Qiao and G. Q. Lu, *Nanoscale*, 2011, **3**, 2801–2818.

23 H. Lee, S. M. Dellatore, W. M. Miller and P. B. Messersmith, *Science*, 2007, **318**, 426–430.

24 M. L. Alfieri, T. Weil, D. Y. W. Ng and V. Ball, *Adv. Colloid Interface Sci.*, 2022, **305**, 102689.

25 Y. M. Tang, Y. Tan, K. L. Lin and M. Zhu, *Front. Chem.*, 2021, **9**, 727123.

26 Y. W. Zhu, Y. J. Sun, J. L. Wang and B. R. Yu, *Rare Met.*, 2022, **41**, 499–518.

27 Q. Chen, X. J. Cao, Z. Y. Jin, Z. E. Yi, B. Chen, J. W. Deng, L. S. Zha, L. Zhang and Z. B. Zha, *Small*, 2025, 21.

28 L. Aguerri, F. Silva and F. Leonardi, *Food Control*, 2025, **178**, 111475.

29 J. F. Tong, L. Meng, C. Bei, Q. Y. Liu, M. Wang, T. T. Yang, H. E. Takiff, S. Y. Zhang, Q. Gao, C. Wang and B. Yan, *Emerg. Microb. Infect.*, 2022, **11**, 715–724.

30 Q. K. Jiang, Y. P. Qiu, I. J. Kurland, K. Drlica, S. Subbian, S. Tyagi and L. B. Shi, *Mbio*, 2022, **13**, e01274.

31 V. M. T. Bart, R. J. Pickering, P. R. Taylor and N. Ipseiz, *Immunology*, 2021, **163**, 128–144.

32 E. Dalle Vedove, G. Costabile and O. M. Merkel, *Adv. Healthcare Mater.*, 2018, **7**, e1701398.

33 H. Bera, C. Z. Zhao, X. D. Tian, D. M. Cun and M. S. Yang, *Pharmaceutics*, 2024, **16**, 429.

34 Y. Song, H. Jiang, B. Wang, Y. Kong and J. Chen, *ACS Appl. Mater. Interfaces*, 2018, **10**, 1792–1801.

35 D. Yu, J. Xu, R. Li, J. Zhao, F. Li, Y. Zhai, J. Xue, H. Song, F. Yang, P. Xu and Y. Song, *ChemistrySelect*, 2021, **6**, 10682–10687.

36 W. Tu, H. Li, B. Li, J. Cheng, P. Xu, W. Zhang, Z. Guo, J. Zhao, F. Li, Y. Song and F. Yang, *J. Alloys Compd.*, 2022, **924**, 166489.

37 M. L. Ferreira, M. Pedernera and M. E. Adrover, *Chem. Eng. J.*, 2024, **498**, 155431.

38 N. Jaber, O. H. Abusara, A. I. M. Ibrahim and M. Al-Remawi, *J. Drug Delivery Sci. Technol.*, 2025, **107**, 106840.

39 Z. Li, H. Li, X. Zeng, S. Liu and Y. Yang, *Chem. Eng. J.*, 2023, **458**, 141455.

40 A. Rousaki and P. Vandenabeele, *J. Raman Spectrosc.*, 2021, **52**, 2178–2189.

41 M. K. Sneha Senapati, N. Singh, S. S. Kulkarni and J. P. Singh, *ACS Appl. Nano Mater.*, 2024, **7**, 6736–6748.

42 S. Ferraris, M. Miola, A. Cochis, B. Azzimonti, L. Rimondini, E. Prenesti and E. Vernè, *Appl. Surf. Sci.*, 2017, **396**, 461–470.

43 X. Yang, X. Niu, Z. Mo, R. Guo, N. Liu, P. Zhao and Z. Liu, *Electrochim. Acta*, 2019, **319**, 705–715.

44 Z. Gong, L. Qian, S. Shao, B. Fan, J. Peng, K. Lu and S. Gao, *Chem. Eng. J.*, 2022, **436**, 135034.

45 W. L. Feng, G. F. Li, X. X. Kang, R. B. Wang, F. Liu, D. D. Zhao, H. F. Li, F. Q. Bu, Y. J. Yu, T. F. Moriarty, Q. Ren and X. Wang, *Adv. Mater.*, 2022, **34**, 2109789.

46 M. V. Nora de Souza, M. d. L. Ferreira, A. C. Pinheiro, M. F. Saraiva, M. V. de Almeida and M. S. Valle, *Sci. World J.*, 2008, **8**, 720–751.

47 P. Kanniah, P. Chelliah, J. R. Thangapandi, G. Gnanadhas, V. Mahendran and M. Robert, *Int. J. Biol. Macromol.*, 2021, **189**, 18–33.

48 C. C. Chen, Y. Y. Chen, C. C. Yeh, C. W. Hsu, S. J. Yu, C. H. Hsu, T. C. Wei, S. N. Ho, P. C. Tsai, Y. D. Song, H. J. Yen, X. A. Chen, J. J. Young, C. C. Chuang and H. Y. Dou, *Front. Pharmacol*, 2021, **12**, 746496.

49 Y. Zhou, Y. Kong, S. Kundu, J. D. Cirillo and H. Liang, *J. Nanobiotechnol.*, 2012, **10**, 19.

50 X. F. Wang, W. J. Hu, Y. H. Zhou, M. Y. Cai, X. L. Wang, K. Lin, C. H. Zhang, S. J. Zhou, H. Pan, L. X. Du and L. J. Xia, *Chem. Eng. J.*, 2025, **522**, 167984.